Check for updates

Influence of tungsten on the NH₃-SCR activity of MnWOₓ/TiO₂ catalysts†

Lu Peng, Li Huan, Liu Huayan, Chen Yinfei and Zhang Zekai *

A series of bulk MnWOₓ and supported MnWOₓ/TiO₂ catalysts with MnWO₄ structure were prepared *via* self-propagating high-temperature synthesis (SHS), co-precipitation and impregnation methods. The catalysts were characterized using X-ray diffraction (XRD), N₂ adsorption/desorption, hydrogen-temperature programmed reduction (H₂-TPR), X-ray photoelectron spectroscopy (XPS) and transmission electron microcopy (TEM). The performance of MnWOₓ and MnWOₓ/TiO₂ and the relation between the tungsten and manganese oxide species in MnWOₓ and MnWOₓ/TiO₂ catalysts were investigated. The supported MnWOₓ/TiO₂ catalysts exhibited the activity improvement of the SCR reaction *via* the promotion of tungsten. The XRD pattern and the TEM images revealed that the presence of tungsten induces the formation of a MnWO₄ oxide phase, thus weakening the interaction between MnO₂ and TiO₂, which is favorable for the specific surface area of MnWOₓ/TiO₂. The MnWO₄ phase also has a positive effect for the activity and N₂ selectivity of MnWOₓ/TiO₂ in the high temperature range. In a feed gas that contains 500 ppm NO, 500 ppm NH₃, 5 vol% O₂ and N₂ as the balance gas, Mn₂WOₓ/TiO₂-SHS shows the best deNOₓ performance and the NOₓ conversion reaches 100% in the temperature range of 130–300 °C under the reaction condition of 30 000 h⁻¹.

1. Introduction

NH₃-SCR is a well-established technology for the removal of nitrogen oxides from stationary and mobile emission sources.[1–3] V₂O₅ based catalysts have also been proven to be very suitable catalysts for the NH₃-SCR process in the temperature window of 350–400 °C.[4–7] Unfortunately, the temperature of exit flue gas is often lower than the work temperature range; this means there is a lot of excess energy cost when the V₂O₅ based catalysts are used. Finding another catalyst system that can work under the temperature of exit flue gas is thereby attractive for many researchers' interest. Many single and mixed transition oxides system have been developed, such as Mn-,[8–10] Fe-[11,12] and Ce-based catalysts.[13,14] MnO₂ based catalysts have been substantially investigated, which are famous for the high activity and poor poison resistance at low temperature range.[15–17]

In the V₂O₅ and CeO₂ based catalysts, tungsten is usually used as a promoter and stabilizer. WO₃ can widen the work temperature window and raise the SO₂ resistance by inhibiting the initial sintering of TiO₂, increasing the amount of Lewis acid over catalyst, improving the electron transfer of the catalyst, facilitating the formation of reduced V₂O₅, and directly providing the active sites[18–21] The promotion effect also have

been adopted to improve the performance of MnO₂ based catalysts.[22–24] Casapu *et al.*[25] screened the doped MnOₓ–CeO₂ catalysts and found that an even stronger suppression of N₂O formation was obtained with MnWCe system, but this catalyst also showed a very low ammonia oxidation activity. Xu *et al.*[26] studied the tungsten modified MnOₓ–CeO₂/ZrO₂ monolith catalysts and found that MnOₓ–CeO₂/10% WO₃–ZrO₂ had the best textural properties and the most adsorbed sites of NH₃ or NO species. The NOₓ conversion was more than 80% in the temperature range of 150 to 380 °C at the gas hourly space velocity of 10 000 h⁻¹. Meanwhile, Peng *et al.*[27] doped CeW catalyst with manganese and found MnCeW system exhibited more activity for NOₓ conversion than the CeW catalyst below 200 °C. The addition of tungsten to Mn/Ce/Ti resulting in the Mn/Ce/W/Ti catalyst also showed excellent NOₓ conversion in the 120–200 °C and SO₂ resistance.[28] These results illuminated the promoting effect of tungsten to the MnO₂ based catalysts. Further, Liu *et al.* first considered the MnWOₓ as the main active phase and got high deNOₓ efficiency from 60 to 250 °C.[29] Sun *et al.*[30] then prepared a series of WₐMn₁₋ₐOₓ Catalysts *via* coprecipitation method. W₀.₃₃Mn₀.₆₆Oₓ catalyst with amorphous or poorly crystalline Mn and W species showed the highest NH₃-SCR activity within a broad temperature range of 230–470 °C. Our group also prepared a MnₓW₀.₀₅Ti₀.₉₅₋ₓO₂₋δ catalyst with self-propagating high-temperature synthesis method and obtained a high activity in the range of 200–400 °C. In different, an uncertain crystal phase was observed on the TEM image, which might be helpful for the activity of the MnWTi catalyst.[31]

Department of Energy Chemical Engineering, Zhejiang University of Technology, Chaowang Road 18, Hangzhou 310014, China. E-mail: zzk@zjut.edu.cn; Tel: +86-571-88320767

In this paper, to discuss the promoting function of tungsten and $MnWO_4$ phase on the properties of MnO_2 based catalysts, a series of bulk and supported $MnWO_x$ catalysts were prepared by self-propagating high-temperature synthesis (SHS), co-precipitation (CP) and impregnation (IMP) methods, and their catalytic activity in NH_3-SCR reaction were tested.

2. Experimental

2.1 Catalyst preparation

The $MnWO_x$ catalysts were mainly prepared by self-propagating high-temperature synthesis, co-precipitation and impregnation method. The general preparation steps are as follows: for the bulk $MnWO_x$ catalysts *via* self-propagating high-temperature synthesis, stoichiometric molar amount of manganous nitrate $(Mn(NO_3)_2 \cdot 4H_2O)$ and ammonium tungstate hydrate $((NH_4)_{10}$-$W_{12}O_{41} \cdot xH_2O)$ was dissolved in the de-ioned water respectively. The total amount of precursor metal-salts is 0.01 mol. 0.1 mol of glycine (CH_2NH_2COOH) was then added into the precursor solution as a fuel. Then, the mixed solution was stirred, heated and concentrated to form proper homogeneity till it burnt. Then, the solid was transferred into a clean crucible and moved into a muffle kept at the constant temperature for 2 h for the aging of the target catalyst. Under the same conditions, the mixed Mn–W oxides catalysts with different molar ratio of Mn to W (labeled as Mn_aWO_x later) were dispersed on the surface of TiO_2 (anatase, htnano Co., Ltd). The loading amount of active components is kept at 20 wt%. The Mn_2WO_x and Mn_2WO_x/TiO_2 catalysts with typical $MnWO_4$ phase were also prepared by co-precipitation and impregnation method. The detailed steps can be seen in elsewhere.[32] As a reference, MnO_2, WO_3, WO_3/TiO_2 (20 wt% WO_3), MnO_2/TiO_2 (20 wt% MnO_2) samples were also prepared *via* self-propagating high-temperature synthesis.

2.2 Catalyst characterization

N_2 adsorption/desorption isotherms of the catalysts were measured at $-196 °C$ using a physical adsorption apparatus (3Flex, Micromeritics) to calculate BET surface area of the catalysts. Prior to measurement, all samples were degassed at $280 °C$ for 10 h to remove the impurities in the porous structure.

The XRD patterns of the samples were checked using an ARL SCINTAG X'TRA X-ray diffractometer (Shimadzu) equipped with $CuK\alpha$ radiation. XRD patterns were recorded in the 2θ range of $10°$ to $80°$ with a scan step size of $0.02°$.

Transmission electron microscopy (TEM) images of the catalysts were taken on a Tecnai G2 F30 S-Twin electron microscope operating at an accelerating voltage of 300 kV. The dispersion of the elemental composition and the semi-quantitative determination of the Ti, Mn, W, and O ratio were detected by the energy dispersive X-ray spectrometer (EDX) at the same time.

The hydrogen temperature programmed reduction (H_2-TPR) profiles of the catalysts were recorded by a chemisorber (Chem2910, Finesorb). Each sample (*ca.* 100 mg) were pretreated at $200 °C$ for 2 h in Ar flow before reduction process. Subsequently, the sample was heated from $100 °C$ to $950 °C$ in 5 vol% H_2/95 vol% Ar flow, at a rate of 30 ml min^{-1} with a heating rate of 10 °C min^{-1}.

X-ray photoelectron spectroscopy (XPS) was used to analyze the surface atomic state and form of catalyst with Al target and $K\alpha$ radiation, operating at 15 kV voltage and C 1s = 284.8 eV for calibration (Kratos AXIS Ultra DLD). The concentrations of Mn, W, Ti and O on catalyst surface were calculated from the peak areas ratios of the samples.

2.3 Catalytic tests

The activity evaluation of the catalysts was carried out in a fixed-bed quartz reactor with an inner diameter of 8 mm. The reaction conditions were as follows: 0.5 g of catalyst (20–60 mesh, 1 ml),500 ppm NO, 500 ppm NH_3, 5 vol% O_2, N_2 as the balance gas, the total gas flow rate was 500 ml min^{-1}, and the corresponding gas hourly space velocity (GHSV) was 30 000 h^{-1}. The catalyst bed temperature was increased gradually and kept at each reaction temperature for half an hour to ensure the stabilization of the reaction. The composition of the feed gases were monitored continuously online using Teledyne T200H/M chemiluminescent NO_x analyzer and gas chromatograph (Thermo Trace 1300 equipped with Porapak Q column). NO_x conversion and N_2 selectivity are calculated as follows: NO_x conversion (%) = $([NO_x]_{in} - [NO_x]_{out})/[NO_x]_{in}$, N_2 selectivity (%) = $(([NO]_{in} + [NH_3]_{in}) - [NO_2]_{out} - 2[N_2O]_{out})/([NO]_{in} + [NH_3]_{in})$.

3. Results and discussions

3.1 Synthesis and characterization of the bulk and supported $MnWO_x$ catalysts

3.1.1 Textual properties of the bulk and supported $MnWO_x$ catalysts. Table 1 lists the textual properties of the bulk $MnWO_x$ catalysts. WO_3 almost has no surface area, which explains its poor catalytic activity. With the increment of Mn : W ratio, the surface area continually increases. MnO_2 has the largest surface area of 30 m^2 g^{-1}. It seems that the existence of tungsten has a negative effect on the surface areas of the $MnWO_x$ catalysts by self-propagating high-temperature synthesis. The lower surface area of the $MnWO_x$ catalysts than the MnO_2 partially explains their worse activities than MnO_2 in low temperature range.

Table 2 lists part of the textual properties of the TiO_2 with supported $MnWO_x$ catalysts. Compared to the bulk $MnWO_x$, the variation of surface area of these samples shows a different way. The Mn_2WO_x/TiO_2-SHS keeps the largest surface area of 142 m^2

Table 1 Textual properties of the bulk $MnWO_x$ catalysts

Samples	BET surface area (m^2 g^{-1})	Pore volume (cm^3 g^{-1})	Average pore diameter (nm)
WO_3-SHS	0	—	—
$MnWO_x$-SHS	5	—	—
Mn_2WO_x-SHS	6	0.0421	28.7
Mn_5WO_x-SHS	15	0.0704	18.3
$Mn_{10}WO_x$-SHS	25	0.156	24.6
MnO_2-SHS	30	0.178	23.5

Table 2 Textual properties of the supported $MnWO_x$ catalysts

Samples	BET surface area $(m^2\ g^{-1})$	Pore volume $(cm^3\ g^{-1})$	Average pore diameter (nm)
WO_3/TiO_2-SHS	109	0.212	7.8
MnO_2/TiO_2-SHS	85	0.194	9.0
Mn_2WO_x/TiO_2-SHS	142	0.217	6.1
TiO_2	184	0.296	6.4

g^{-1}; while the MnO_2/TiO_2-SHS only has 85 $m^2\ g^{-1}$ of BET surface area, which is even smaller than 109 $m^2\ g^{-1}$ of WO_3/TiO_2-SHS. The results means that the existence of W can alleviate the decrement of TiO_2 surface area, and increase the BET surface area of $MnWO_x/TiO_2$-SHS. Further, the decrement of average pore diameter of Mn_2WO_x/TiO_2-SHS indicates that the Mn_2WO_x species are well dispersed in the pore structure of TiO_2, which will be favorable for the activity.

3.1.2 XRD patterns of the $MnWO_x$ catalysts. Fig. 1 displays the XRD patterns of the bulk and supported $MnWO_x$ catalysts. The bulk $MnWO_x$ samples do not have characteristic peaks of MnO_2. Instead, they mainly present the typical characteristic peaks of monoclinic structure phase of $MnWO_4$.[32] A little part of Mn_3O_4 also can be found on the pattern of $MnWO_x$ sample. The
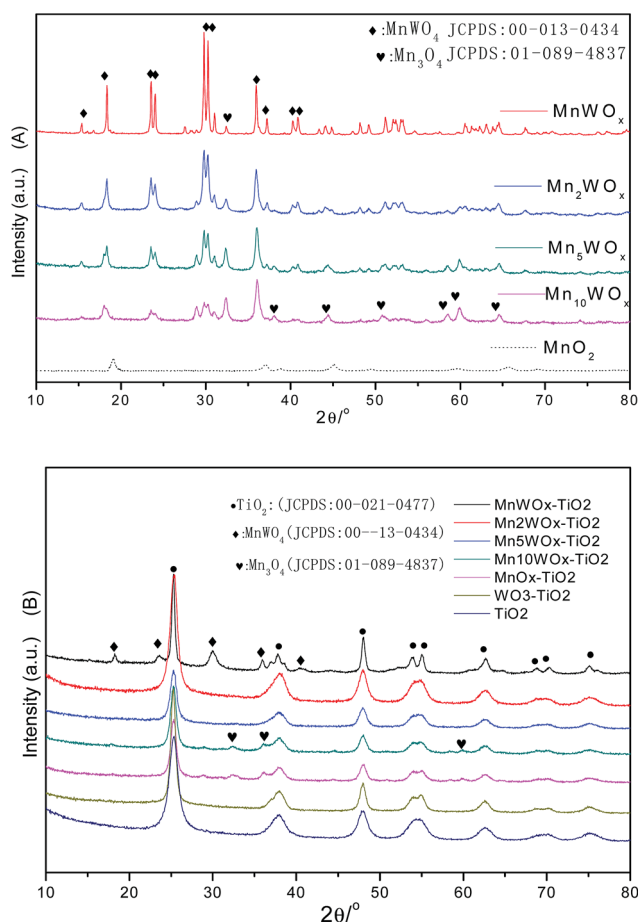
peaks intensity of Mn_3O_4 and $MnWO_4$ gradually enhance with the increment of Mn : W ratio. It means that the main species were the $MnWO_4$ and the Mn_3O_4 on the bulk $MnWO_x$. The general valence of manganese in $MnWO_x$ catalysts has been suppressed to be about +2/+3. In Fig. 1B, the TiO_2 with supported WO_3 (WO_3/TiO_2) sample only presented the characteristic peaks of anatase TiO_2. The MnO_2/TiO_2 and $Mn_{10}WO_x/TiO_2$ presents the characteristic peaks of Mn_3O_4 and anatase TiO_2. The $MnWO_x/TiO_2$ presents the characteristic peaks of $MnWO_4$ and anatase TiO_2. However, the characteristic peaks of $MnWO_4$ and Mn_3O_4 disappeared together on the patterns of Mn_2WO_x/TiO_2 and Mn_5WO_x/TiO_2, which can be ensured that the active species were well dispersed on the TiO_2. The above results suggested that the coexistence of $MnWO_4$ and Mn_3O_4 weaken the intensity of characteristic peaks and caused the disappearances of $MnWO_4$ and Mn_3O_4 on the patterns of Mn_2WO_x/TiO_2 and Mn_5WO_x/TiO_2. For the $MnWO_x$ catalysts, $MnWO_4$ phase seemed to play an important role in NH_3-SCR reaction.

3.1.3 H_2-TPR of TiO_2 with supported $MnWO_x$ samples with self-propagating high-temperature synthesis. The NH_3-SCR activity of $MnWO_x$ has a strong relation with the redox properties in the SCR reaction. H_2-TPR was performed to identify the active species on the $MnWO_x$ catalysts. Fig. 2 displays the profiles of different supported $MnWO_x/TiO_2$ samples and quantitative results are summarized in Tables S1 and S2.† It is known that the reduction of manganese oxides is influenced by the support properties, dopants, the preparation method as well as the reduction conditions.[33] Here, the profiles seems to be some complicated. In general, for the supported $MnWO_x/TiO_2$ samples with SHS method, the profile can be divided into two reduction bands. In the lower temperature range of 200–500 °C, the reduction peaks are mainly originated from different MnO_x species; in the higher temperature range of 600–900 °C, the reduction peaks are from different WO_x species.[34,35] For the four reduction peaks in 200–500 °C on the MnO_2/TiO_2 profile, the peaks at about 300, 400 and 460 °C can be attributed to the reduction of MnO_2 to Mn_2O_3, Mn_2O_3 to Mn_3O_4 and Mn_3O_4 to

Fig. 1 XRD patterns of bulk and supported $MnWO_x$ catalysts.
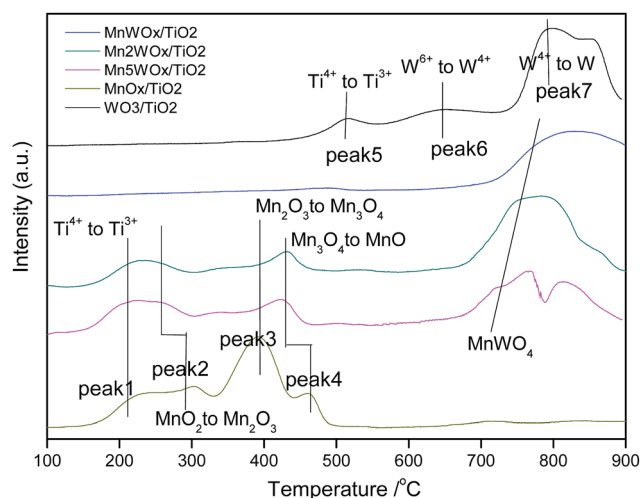
Fig. 2 H_2-TPR profiles of different TiO_2 with supported $MnWO_x$ samples with different Mn : W ratio and preparation methods.

MnO, respectively. Besides that, the peak at 220 °C is from the reduction of part Ti^{4+} to Ti^{3+}, which have interaction with manganese oxides.[33] The reduction profiles of Mn_aWO_x/TiO_2-SHS are clearly different from MnO_2/TiO_2. The reduction peaks of manganese oxides are almost diminished on the $MnWO_x/TiO_2$-SHS, which indicates that all the manganese species are well interacted with the tungsten and form the $MnWO_x$ structure. The reduction peaks in 200–500 °C appear again on the Mn_2WO_x/TiO_2-SHS and Mn_5WO_x/TiO_2-SHS, indicates that excess manganese oxides are existed on the samples other than $MnWO_x$. The reduction peak sites move to the lower temperature attitude, and the peak intensity of Mn_2O_3 to Mn_3O_4 clearly decreases. Under this conditions, it seems that the MnO_2 species are easy to be reduced and the large part of MnO_2 can be directly reduced to MnO.

Another main reduction band distributed in 600–900 °C is probably from tungsten oxides, $MnWO_4$ species and titanium oxides.[36,37] For WO_3/TiO_2 sample, the reduction peaks at 520 °C, 650 °C and 800 °C are most probably from part of Ti^{4+} to Ti^{3+}, W^{6+} to W^{4+} and W^{4+} to W^0.[38,39] When manganese is added, the two peaks at 520 °C and 650 °C diminished on the Mn_aWO_x/TiO_2-SHS profiles. The diminishing of peak at 520 °C might indicate the excellent dispersion of $MnWO_4$ on the surface of TiO_2 support; the diminishing of peak at 650 °C represents that there is no single WO_3 species left. The only peak around 790 °C should be from $MnWO_4$ structure, and it can be inferred that the Mn^{4+} and W^{6+} in $MnWO_4$ structure needs a high temperature to be reduced. With the manganese content increases, the reduction temperature seems to be decreased.

3.1.4   TEM of the bulk $MnWO_x$ and supported $MnWO_x$/ TiO_2 samples by self-propagating high-temperature synthesis. TEM images can distinguish the existence of the crystal structures in some areas. Fig. 3 displays the TEM images of the bulk and supported $MnWO_x$ catalysts with different preparation methods. Co-precipitation method gets the homogenous particles with typical regular nano-rod shapes of $MnWO_4$ structure in Fig. 3a. The ordered lattice fringes in Fig. 3b confirm that the particles have a typical $MnWO_4$ crystal structure. 0.487 nm and 0.379 nm lattice spacing belongs to crystal face (100) and face (011) of $MnWO_4$.[40] On the Mn_2WO_x-SHS, the uniform lattice fringes with 0.483 nm of face (100) and 0.245 nm of face (200) can be seen in Fig. 3d. The rectangular shaped electron diffraction pattern also can confirm the $MnWO_4$ structure. The agglomeration of particles clearly happens on the sample, which causes the poor specific area and poor NH_3-SCR activity.

For the two supported samples, $MnWO_x$ species are uniformly distributed on the surfaces of the two samples in the shape of about 1 nm diameter nanoparticles, which are shown as the little black dots in Fig. 3f and h. Partly due to the little sizes of the nanoparticles, $MnWO_4$ phase is hard to be distinguished on the images. The main change is come from the TiO_2 support. It looks like that the TiO_2 support has grown into large plates *via* impregnation method (Fig. 3e). The specific surface area of Mn_2WO_x/TiO_2-IMP is thereby severely influenced and decreases from 184 $m^2\ g^{-1}$ to 56 $m^2\ g^{-1}$, which may cause the activity decreases. Meanwhile, the self-propagating high-
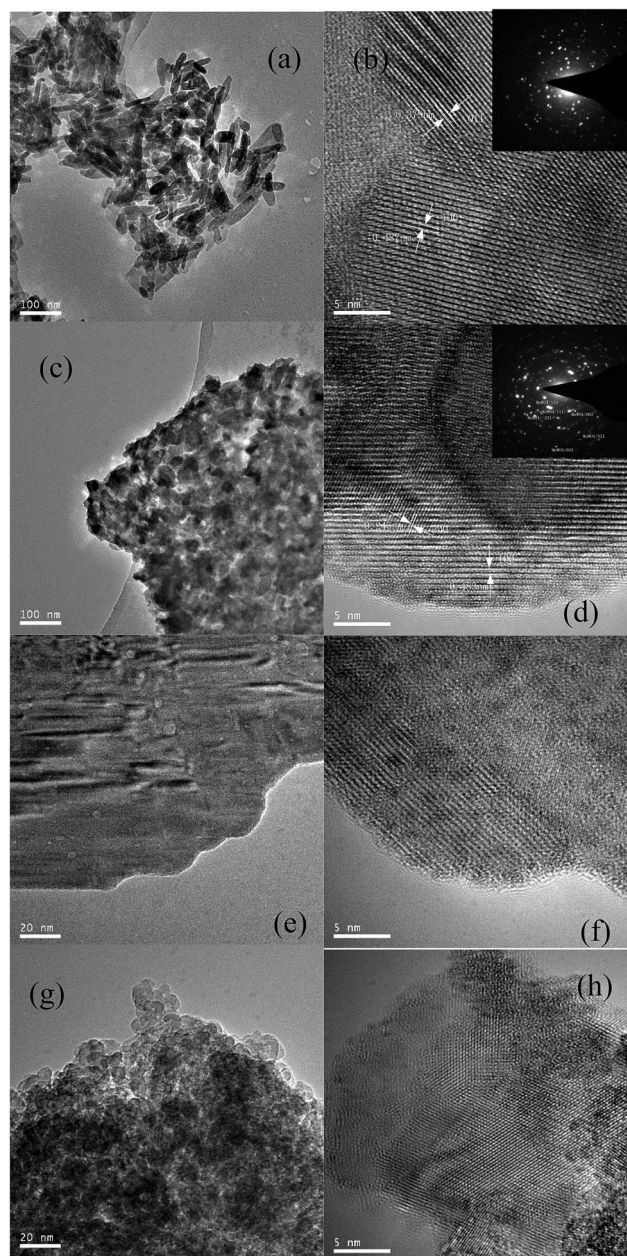

Fig. 3 TEM images of the bulk and supported $MnWO_x$ catalysts with different preparation methods. (a), (b): Mn_2WO_x-CP; (c), (d): Mn_2WO_x-SHS; (e), (f): Mn_2WO_x/TiO_2-IMP; (g), (h) Mn_2WO_x/TiO_2-SHS.

temperature synthesis method keeps the structure of TiO_2 support much better and more $MnWO_x$ species nanoparticles can be formed and seen on the surface.

3.1.5   Characterization of the bulk and supported $MnWO_x$ samples by XPS method. Oxidation states and atomic concentrations of manganese can reflect the properties of manganese species over the series of catalysts. XPS have been conducted for the $MnWO_x$-CP, $MnWO_x/TiO_2$-IMP, Mn_2WO_x-SHS and Mn_2WO_x/TiO_2-SHS. All binding energies presented have been adjusted *via* the C 1s peak standardized at 284.8 eV. The XPS spectra of Mn 2p are shown in Fig. 4. Two XPS peaks of Mn 2p appear at about 641.8 and 653.8 eV belonging to Mn $2p_{3/2}$ and Mn $2p_{1/2}$
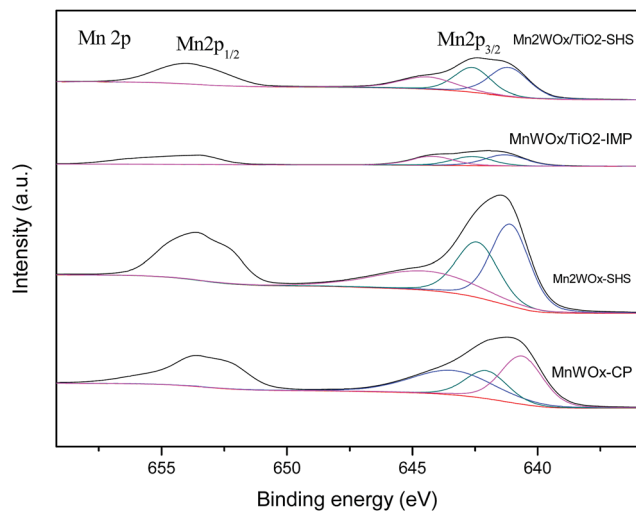
Fig. 4 Mn 2p XPS spectra of $MnWO_x$-CP, $MnWO_x/TiO_2$-IMP, Mn_2WO_x-SHS and Mn_2WO_x/TiO_2-SHS.

Fig. 5 O 1s XPS spectra of $MnWO_x$-CP, $MnWO_x/TiO_2$-IMP, Mn_2WO_x-SHS and Mn_2WO_x/TiO_2-SHS.

respectively. The Mn $2p_{3/2}$ spectra of all catalysts can be fitted into three sub-bands by Gaussian deconvolution. The peaks at 640.6–641.4 eV can be attributed to Mn^{3+}, the peaks at 642.0–642.6 eV to Mn^{4+}, and the peaks at 643.4–644.5 eV to Mn^{2+}.[28,29,41,42] According to quantitative results in the Table 3, the Mn^{3+} and Mn^{2+} ions took the main part of manganese species. The average valence of manganese has been drawn to be +2.8, +3.0, +3.0 and +3.2 on the four catalysts. Among the four catalysts, the average valence of manganese is the lowest and the composition of Mn^{2+} is the highest, which suggests the valence restriction from the formation of $MnWO_4$ phase.

Oxygen species plays an important role in the NH_3-SCR activity. The O 1s XPS of Mn_aWO_x and Mn_aWO_x/TiO_x are thereby displayed in Fig. 5, and the characteristic peaks are deconvoluted by Gaussian fitting method. The sub-bands at 528.9–530.4 eV can be attributed to the lattice O^{2-} (denoted as O_β); the sub-bands with higher binding energy at 531.0–531.5 eV to surface absorbed oxygen (denoted as O_α) such as O_2^{2-} and O^- belonging to defect-oxide or hydroxyl-like group, and the binding energy at 532.3–533.2 eV can be assigned to chemisorbed water (denoted as $O_{\alpha'}$).[43–46] The surface absorbed O_α is usually regard as more reactive in oxidation reactions due to its higher mobility than lattice O^{2-}, which is also beneficial to the NO oxidation to NO_2 thus facilitating the "fast SCR" process. The ratios of O_α, O_β and $O_{\alpha'}$ on four catalysts are calculated and listed in Table 4. The bulk $MnWO_x$ and Mn_2WO_x catalysts have

high O_α ratios of 31.78% and 34.72% respectively, which means that the Mn_aWO_x mixed oxides may have a high response to the NH_3-SCR reaction. The poor performance in Fig. 6 may be caused by the poor BET surface area. When the specific surface area is increased by TiO_2 supporting, Mn_aWO_x/TiO_2 then shows the high activity in NH_3-SCR reaction.

3.2 Catalytic activity of the bulk and supported $MnWO_x$ catalysts

Fig. 6A displayed the activities of the bulk $MnWO_x$ catalysts with different Mn : W ratio by self-propagating high-temperature synthesis. Due to the poor specific surface area, the bulk WO_3 did not show the NH_3-SCR activity obviously; while the bulk

Table 4 Quantitative results of O 1s XPS spectra of $MnWO_x$-CP, $MnWO_x/TiO_2$-IMP, Mn_2WO_x-SHS and Mn_2WO_x/TiO_2-SHS

Samples	O_β BE (eV)	Per.%	O_α BE (eV)	Per.%	$O_{\alpha'}$ BE (eV)	Per.%
$MnWO_x$-CP	530.2	55.20	531.4	31.78	533.1	13.02
Mn_2WO_x-SHS	530.4	41.06	531.0	34.72	532.8	24.22
$MnWO_x/TiO_2$-IMP	530.0	47.68	531.5	26.75	532.9	25.57
Mn_2WO_x/TiO_2-SHS	528.9	57.67	531.2	24.65	532.3	17.68

Table 3 Quantitative results of Mn 2p XPS spectra of $MnWO_x$-CP, $MnWO_x/TiO_2$-IMP, Mn_2WO_x-SHS and Mn_2WO_x/TiO_2-SHS

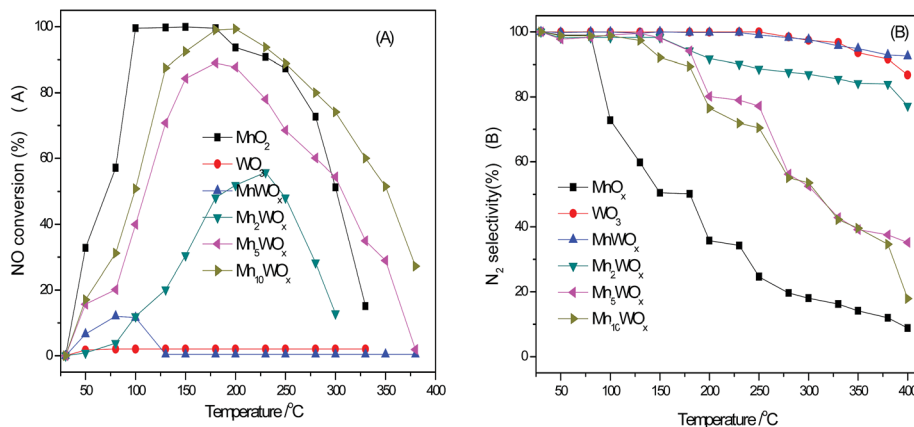| Samples	Mn^{4+} BE (eV)	Per.%	Mn^{3+} BE (eV)	Per.%	Mn^{2+} BE (eV)	Per.%	Average valence
$MnWO_x$-CP	642.0	22.32	640.6	38.85	643.4	38.83	2.8
Mn_2WO_x-SHS	642.4	31.08	641.1	42.38	644.5	26.54	3.0
$MnWO_x/TiO_2$-IMP	642.6	30.26	641.3	38.17	644.2	31.57	3.0
Mn_2WO_x/TiO_2-SHS	642.6	33.26	641.1	42.37	644.4	24.37	3.1

Fig. 6 (A) NO conversion and (B) N_2 selectivity over bulk MnO_2, WO_3 and $MnWO_x$ catalysts. Reaction conditions: $[NO] = [NH_3] = 500$ ppm, $[O_2] = 5$ vol%, N_2 balance gas and GHSV = 30 000 h^{-1}.

MnO_2 with the largest specific surface area among all the bulk samples showed the best performance in the lower temperature range. 100% NO_x conversion had been achieved in the range of 100–180 °C. When the W and Mn coexist and form the series of Mn_aWO_x catalysts, the activity catalysts undergone a series of change. Mn_1WO_x only showed poor activity in the range of 50–120 °C. Mn_2WO_x displayed higher activity in the temperature range of 100–300 °C. With the continuous increment of Mn content, the activity of Mn_aWO_x did not surpass the bulk MnO_2 in the low temperature, some of Mn_aWO_x samples with high Mn : W ratio behaved better performance in the high temperature range. The $Mn_{10}WO_x$ exhibited the higher activity than the bulk MnO_2 when the reaction temperature is above 200 °C.

The N_2 selectivities of bulk $MnWO_x$ catalysts with different Mn : W ratio are presented in Fig. 6B. It can be seen that tungsten has a clearly effect of $MnWO_x$ on the N_2 selectivity, especially in the high temperature range. The N_2 selectivity of bulk MnO_2 decreases to be about 20% when the temperature rise to 200 °C. While with the decrease of Mn : W ratio, i.e., the increases of W content, the N_2 selectivity of Mn_aWO_x is more and more improved. On the $MnWO_x$ with 1 : 1 ratio, the N_2 selectivity of has almost reached 100%, the insertion of tungsten into Mn_aWO_x favours the increase in the activity and N_2 selectivity. Supported $MnWO_x/TiO_2$ catalysts with high specific surface area were then prepared and the activities were tested under the same reaction conditions. As shown in Fig. 7A and B, the supporting of MnO_2 did not improve the activity of MnO_2/TiO_2. The 100% NO_x conversion window (working window) was still in the range of 100–180 °C. Meanwhile, the Mn_aWO_x/TiO_2 catalysts showed much better performance than the bulk Mn_aWO_x samples and single MnO_2 catalysts. Except Mn_1WO_x/TiO_2, all the other Mn_aWO_x/TiO_2 catalysts presented the 100% NO_x conversion temperature window. The temperature window of the $Mn_{1.5}WO_x/TiO_2$ was 180–240 °C; The Mn_2WO_x/TiO_2 was 130–300 °C, and the window of Mn_5WO_x/TiO_2 and $Mn_{10}WO_x/TiO_2$ was in the same range of 130–240 °C.

N_2 selectivity of the supported $MnWO_x$ catalysts are also been improved from Fig. 7C and D. The appearance of N_2 selectivity decrease is retarded to high temperature attitude,

and the decrease degree is alleviated with the Mn : W ratio decreasing. On the Mn_aWO_x/TiO_2 with Mn : W ratio of 1 and 2, N_2O is only formed above 200 °C and the N_2 selectivity of $Mn_{1-2}WO_x/TiO_2$ catalysts keep above 80% during the course.

The results show that the addition of tungsten can improve the activity and N_2 selectivity of supported MnO_2 based catalysts, especially in the higher temperature range. Though the Mn_1WO_x/TiO_2 does not achieve the 100% NO_x conversion, it shows much better activity than the MnO_2/TiO_2 when the temperature is above 250 °C. When the Mn : W ratio increases to 2 : 1, the performance of Mn_aWO_x/TiO_2 will be better than MnO_2/TiO_2. It is the Mn_2WO_x/TiO_2 that fetches the best performance among all the Mn_aWO_x/TiO_2 samples. Considering the XRD pattern and BET surface areas, the existence of tungsten have shown two effects on the TiO_2 supported Mn_aWO_x catalysts. The first is that the tungsten can alleviate the specific surface area loss of TiO_2 support. The BET surface area of Mn_2WO_x/TiO_2-SHS is clearly bigger than WO_3/TiO_2 and MnO_2/TiO_2, which is favorable for the catalytic activity in NH_3-SCR reaction. The second effect may be that the tungsten can interact with manganese oxide and form the $MnWO_4$ phase with manganese oxides, which is even favorable for the catalytic activity.

3.3 Activity of Mn_2WO_x-CP, Mn_1WO_x/TiO_2-IMP and Mn_2WO_x/TiO_2-IMP catalysts

The above results show that tungsten addition can improve NH_3-SCR activities of $MnWO_x$ catalysts. To discuss the mechanism of the addition of tungsten, especially the $MnWO_4$ phase on the catalytic activity. Co-precipitation and impregnation method, which have been reported to be able to get $MnWO_x$ catalysts with typical $MnWO_4$ phase,[32] were used to prepare a bulk Mn_2WO_x (labeled as Mn_2WO_x-CP) and the TiO_2 supported $MnWO_x$ and Mn_2WO_x (labeled as $MnWO_x/TiO_2$-IMP and Mn_2WO_x/TiO_2-IMP). The BET surface areas of Mn_2WO_x-CP, $MnWO_x/TiO_2$-IMP and Mn_2WO_x/TiO_2-IMP are 26, 52 and 56 m^2 g^{-1} respectively. The XRD patterns in Fig. 8 show that both Mn_2WO_x-CP and Mn_2WO_x/TiO_2-IMP both have typical
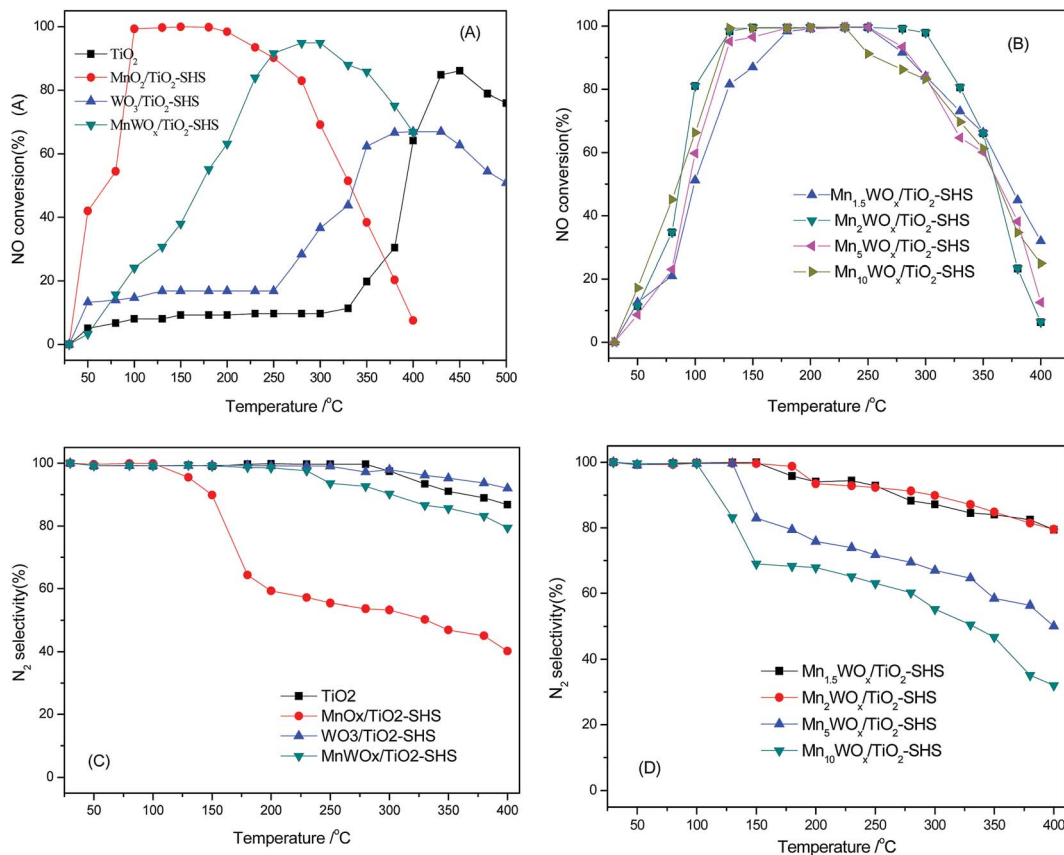
Fig. 7 (A), (B) NO conversion and (C), (D) N₂ activity over supported Mn$_a$WO$_x$/TiO$_2$, MnO$_2$ and WO$_3$ via self-propagating high-temperature synthesis. Reaction conditions: [NO] = [NH$_3$] = 500 ppm, [O$_2$] = 5 vol%, N$_2$ balance gas and GHSV = 30 000 h^{-1}.
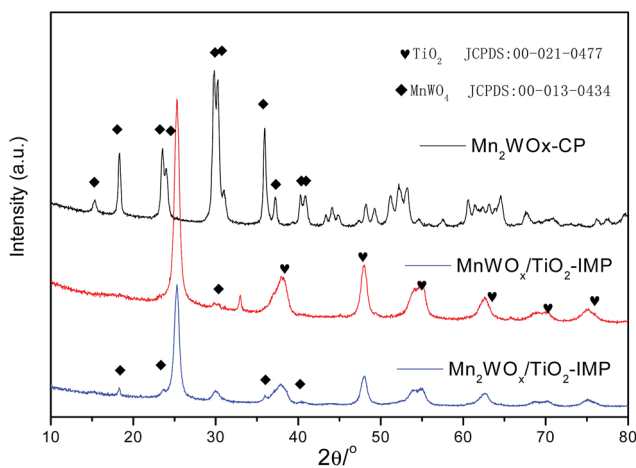

Fig. 8 XRD patterns of Mn$_2$WO$_x$-CP and Mn$_2$WO$_x$/TiO$_2$-IMP.

characteristic peaks of MnWO$_4$ without other impurity phase observed. Otherwise, MnWO$_x$/TiO$_2$-IMP also have MnWO$_4$ structure.

As shown in Fig. 9A, the above three samples exhibit distinctive catalytic performances, compared to the samples with self-propagating high-temperature synthesis method, the main function temperature range of Mn$_2$WO$_x$-CP, MnWO$_x$/

TiO$_2$-IMP and Mn$_2$WO$_x$/TiO$_2$-IMP seemed to move to the high temperature attitude clearly. The NO$_x$ conversion over Mn$_2$WO$_x$-CP continually increased till 430 °C, where it reached the maximum of 52.9%. For the two supported samples, the active temperature window of MnWO$_x$/TiO$_2$-IMP was in the range of 230–350 °C, where it can convert more than 94% NO. The deNO$_x$ performance of MnWO$_x$/TiO$_2$-IMP was better than MnWO$_x$/TiO$_2$-SHS. The activity window of Mn$_2$WO$_x$/TiO$_2$-IMP is similar to MnWO$_x$/TiO$_2$-IMP, which the NO$_x$ conversion can reach 100% in the range of 250–350 °C. But the window width was some narrower than that of Mn$_2$WO$_x$/TiO$_2$-SHS, and moved about 50 °C towards high attitude. Considering the working windows of the two samples, it seems that the working window of MnWO$_x$/TiO$_2$ catalysts can be broadened as wide as 130–350 °C (or even high[31]) by fine tuning or combing of different preparation methods. It also can be inferred that the MnWO$_4$ should have some positive effect on the activity of MnWO$_x$ catalysts, especially for the activity of MnWO$_x$/TiO$_2$-IMP in the high temperature range.

The plot of N$_2$ product selectivity over above three catalysts as a function of temperature is shown in Fig. 9B. Mn$_2$WO$_x$-CP showed an excellent N$_2$ selectivity than MnWO$_x$/TiO$_2$-IMP and Mn$_2$WO$_x$/TiO$_2$-SHS under the range of 250 °C. In contrast, Mn$_2$WO$_x$/TiO$_2$-IMP and Mn$_2$WO$_x$/TiO$_2$-SHS show a better N$_2$ selectivity than Mn$_2$WO$_x$-CP when the temperature is high than
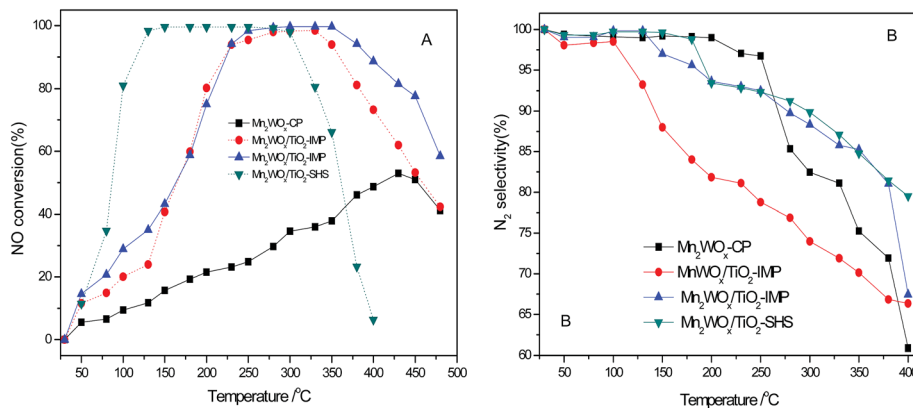
Fig. 9 (A) NO conversion and (B) N_2 selectivity over bulk and supported Mn_2WO_x/TiO_2 with different methods. Reaction conditions: [NO] = [NH$_3$] = 500 ppm, [O$_2$] = 5 vol%, N_2 balance gas and GHSV = 30 000 h^{-1}.

280 °C. It confirms that the improvement of N_2 selectivity is associated with existence of MnWO$_4$ and dispersion on the surface of carrier.

4.   Conclusions

A series of bulk MnWO$_x$ and supported MnWO$_x$/TiO$_2$ catalysts have been prepared by self-propagating high-temperature synthesis, impregnation and co-precipitation method to discuss the effect and mechanism of tungsten on the manganese oxide based catalysts. The tungsten can interact with manganese oxide, thus weaken the interaction between tungsten and titanium or manganese and titanium, alleviate the specific surface area loss of TiO$_2$ support, and improve the NH$_3$-SCR activity of MnWO$_x$/TiO$_2$ catalysts. The tungsten and manganese also can form a MnWO$_4$ crystal structure, which might be favorable for the activity and N_2 selectivity in the high temperature range (above 260 °C). How the MnWO$_4$ works needs to be further investigated. Both self-propagating high-temperature synthesis and impregnation can get uniformly distributed MnWO$_x$ nanoparticles, while the TiO$_2$ support structure is more influenced by impregnation.

Notes and references

1 M. Fu, C. Li, P. Lu, L. Qu, M. Zhang, Y. Zhou, M. Yu and Y. Fang, *Catal. Sci. Technol.*, 2014, **4**, 14–25.

2 F. Can, X. Courtois, S. Royer, G. Blanchard, S. Rousseau and D. Duprez, *Catal. Today*, 2012, **197**, 144–157.

3 Z. Liu, J. Li and J. Hao, *Chem. Eng. J.*, 2010, **165**, 420–425.

4 G. Coudurier and J. C. Védrine, *Catal. Today*, 2000, **56**, 415–430.

5 L. J. Alemany, F. Berti, G. Busca, G. Ramis, D. Robba, G. P. Toledo and M. Trombetta, *Appl. Catal., B*, 1996, **10**, 299–311.

6 L. Lietti, I. Nova, G. Ramis, L. Dall'Acqua, G. Busca, E. Giamello, P. Forzatti and F. Bregani, *J. Catal.*, 1999, **187**, 419–435.

7 D. Ye, R. Qu, H. Song, X. Gao, Z. Luo, M. Ni and K. Cen, *Chem. Eng. J.*, 2016, **283**, 846–854.

8 S. Andreoli, F. A. Deorsola, C. Galletti and R. Pirone, *Chem. Eng. J.*, 2015, **278**, 174–182.

9 J. Xiang, L. Wang, F. Cao, K. Qian, S. Su, S. Hu, Y. Wang and L. Liu, *Chem. Eng. J.*, 2016, **302**, 570–676.

10 C. Liu, J. Shi, C. Gao and C. Niu, *Appl. Catal., A*, 2016, **25**, 54–69.

11 X. Xiong, C. Wu, Q. Hu, Y. Wang, J. Jin, C. Lu and D. Guo, *Chem. Eng. J.*, 2016, **286**, 459–466.

12 R. Foo, T. Vazhnova, D. B. Lukyanov, P. Millington, J. Collier, R. Rajaram and S. Golunski, *Appl. Catal., B*, 2015, **162**, 174–179.

13 D. W. Kwon, K. B. Nam and S. C. Hong, *Appl. Catal., B*, 2015, **166–167**, 37–44.

14 Y. Peng, K. Li and J. Li, *Appl. Catal., B*, 2015, **140–141**, 483–492.

15 D. K. Pappas, T. Boningari, P. Boolchand and P. G. Smirniotis, *J. Catal.*, 2016, **334**, 1–13.

16 Y. J. Kim, H. J. Kwon, I.-S. Nam, J. W. Choung, J. K. Kil, H. J. Kim, M. S. Cha and G. K. Yeo, *Catal. Today*, 2010, **151**, 244–250.

17 S. M. Lee, K. H. Park and S. C. Hong, *Chem. Eng. J.*, 2012, **195–196**, 323–331.

18 S. Zhang and Q. Zhong, *J. Mol. Catal. A: Chem.*, 2013, **373**, 108–113.

19 Y. He, M. E. Ford, M. Zhu, Q. Liu, Z. Wu and I. E. Wachs, *Appl. Catal., B*, 2016, **188**, 123–133.

20 Z. Li, J. Li, S. Liu, X. Ren, J. Ma, W. Su and Y. Peng, *Catal. Today*, 2015, **258**, 11–16.

21 W. Shan, F. Liu, H. He, X. Shi and C. Zhang, *Appl. Catal., B*, 2012, **115–116**, 100–106.

22 Z. Ma, X. Wu, Y. Feng, Z. Si and D. Weng, *Catal. Commun.*, 2015, **69**, 188–192.

23 Z. Liu, Y. Liu, Y. Li, H. Su and L. Ma, *Chem. Eng. J.*, 2016, **283**, 1044–1050.

24 X. Wang, X. Li, Q. Zhao, W. Sun, M. Tade and S. Liu, *Chem. Eng. J.*, 2016, **288**, 216–222.

25 M. Casapu, O. Kröcher and M. Elsener, *Appl. Catal., B*, 2009, **88**, 413–419.

26 H. Xu, Q. Zhang, C. Qiu, T. Lin, M. Gong and Y. Chen, *Chem. Eng. Sci.*, 2012, **76**, 120–128.

27 Y. Peng, Z. Liu, X. Niu, L. Zhou, C. Fu, H. Zhang, J. Li and W. Han, *Catal. Commun.*, 2012, **19**, 127–131.

28 D. W. Kwon, K. B. Nam and S. C. Hong, *Appl. Catal., A*, 2015, **497**, 160–166.

29 F. Liu, W. Shan, Z. Lian, L. Xie, W. Yang and H. He, *Catal. Sci. Technol.*, 2013, **3**, 2699–2707.

30 W. Sun, X. Li, Q. Zhao, M. Tade and S. Liu, *Energy Fuels*, 2016, **30**, 1810–1814.

31 Z. Kong, C. Wang, Z. Ding, Y. Chen and Z. Zhang, *Catal. Commun.*, 2015, **64**, 27–31.

32 J. Tang, J. Shen, N. Li and M. Ye, *J. Alloys Compd.*, 2016, **666**, 15–22.

33 P. R. Ettireddy, N. Ettireddy, S. Mamedov, P. Boolchand and P. G. Smirniotis, *Appl. Catal., B*, 2007, **76**, 123–134.

34 D. Fang, J. Xie, H. Hu, H. Yang, F. He and Z. Fu, *Chem. Eng. J.*, 2015, **271**, 23–30.

35 P. G. W. A. Kompio, A. Brückner, F. Hipler, G. Auer, E. Löffler and W. Grünert, *J. Catal.*, 2012, **286**, 237–247.

36 D. W. Kwon and S. C. Hong, *Appl. Surf. Sci.*, 2015, **356**, 181–190.

37 L. Chen, J. Li and M. Ge, *J. Phys. Chem. C*, 2009, **113**, 21177–21184.

38 C. Wang, S. Yang, H. Chang, Y. Peng and J. Li, *Chem. Eng. J.*, 2013, **225**, 520–527.

39 S. S. R. Putluru, L. Schill, A. Godiksen, R. Poreddy, S. Mossin, A. D. Jensen and R. Fehrmann, *Appl. Catal., B*, 2016, **183**, 282–290.

40 M. Mączka, M. Ptak, M. Kurnatowska, L. Kępiński, P. Tomaszewski and J. Hanuza, *J. Solid State Chem.*, 2011, **184**, 2446–2457.

41 Y. Wan, W. Zhao, Y. Tang, L. Li, H. Wang, Y. Cui, J. Gou, Y. Li and J. Shi, *Appl. Catal., B*, 2014, **148–149**, 2114–2122.

42 Z. Lian, F. Liu, H. He, X. Shi, J. Mo and Z. Wu, *Chem. Eng. J.*, 2014, **250**, 390–398.

43 M. Kang, E. D. Park, J. M. Kim and J. E. Yie, *Appl. Catal., A*, 2007, **327**, 261–269.

44 J. Fang, X. Bi, D. Si, Z. Jiang and W. Huang, *Appl. Surf. Sci.*, 2007, **253**, 8952–8961.

45 W. Shan, F. Liu, H. He, X. Shi and C. Zhang, *Appl. Catal., B*, 2012, **115–116**, 100–106.

46 Z. Kong, C. Wang, Z. Ding, Y. Chen and Z. Zhang, *J. Fuel Chem. Technol.*, 2014, **42**, 1447–1454.